

Dalton Transactions

Accepted Manuscript

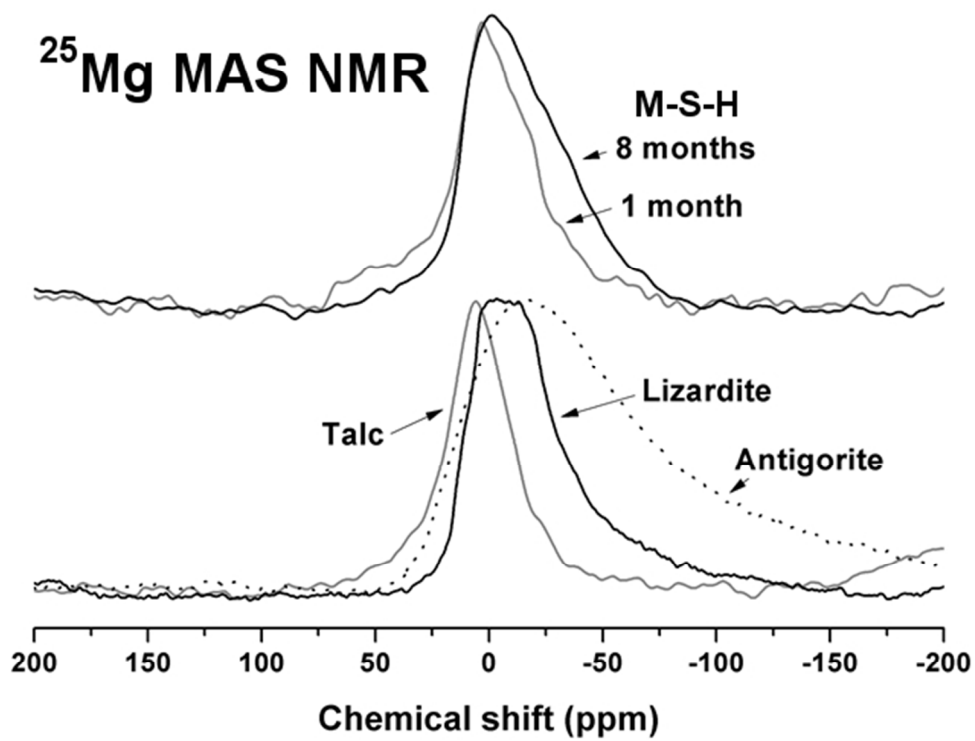


This is an *Accepted Manuscript*, which has been through the Royal Society of Chemistry peer review process and has been accepted for publication.

Accepted Manuscripts are published online shortly after acceptance, before technical editing, formatting and proof reading. Using this free service, authors can make their results available to the community, in citable form, before we publish the edited article. We will replace this *Accepted Manuscript* with the edited and formatted *Advance Article* as soon as it is available.

You can find more information about *Accepted Manuscripts* in the [Information for Authors](#).

Please note that technical editing may introduce minor changes to the text and/or graphics, which may alter content. The journal's standard [Terms & Conditions](#) and the [Ethical guidelines](#) still apply. In no event shall the Royal Society of Chemistry be held responsible for any errors or omissions in this *Accepted Manuscript* or any consequences arising from the use of any information it contains.



231x182mm (72 x 72 DPI)

Magnesium silicate hydrate gels, synthesised for nuclear waste immobilisation, are shown by NMR spectroscopy to be structurally similar to lizardite

1 **Structure and properties of binder gels formed in the system**
2 **Mg(OH)₂-SiO₂-H₂O for immobilisation of Magnox sludge**

3
4 Sam A. Walling¹, Hajime Kinoshita¹, Susan A. Bernal¹, Nick C. Collier^{1,2}, John L. Provis^{1*}

5
6 ¹ *Immobilisation Science Laboratory, Department of Materials Science & Engineering, The*
7 *University of Sheffield, Sheffield, S1 3JD, United Kingdom*

8 ² *National Nuclear Laboratory, Chadwick House, Warrington Road, Birchwood Park,*
9 *Warrington, WA3 6AE, United Kingdom*

10
11 * *Corresponding author. Tel: +44 (0) 114 222 5490, email: j.provis@sheffield.ac.uk*

12
13 **Abstract**

14 A cementitious system for the immobilisation of magnesium rich Magnox sludge was
15 produced by blending an Mg(OH)₂ slurry with silica fume and an inorganic phosphate
16 dispersant. The Mg(OH)₂ was fully consumed after 28 days of curing, producing a disordered
17 magnesium silicate hydrate (M-S-H) with cementitious properties. The structural
18 characterisation of this M-S-H phase by ²⁹Si and ²⁵Mg MAS NMR showed clearly that it has
19 strong nanostructural similarities to a disordered form of lizardite, and does not take on the
20 talc-like structure as has been proposed in the past for M-S-H gels. The addition of sodium
21 hexametaphosphate (NaPO₃)₆ as a dispersant enabled the material to be produced at a much
22 lower water/solids ratio, while still maintaining the fluidity which is essential in practical
23 applications, and producing a solid monolith. Significant retardation of M-S-H formation was
24 observed with larger additions of phosphate, however the use of 1 wt. % (NaPO₃)₆ was
25 beneficial in increasing fluidity without a deleterious effect on M-S-H formation. This work
26 has demonstrated the feasibility of using M-S-H as binder to structurally immobilise Magnox
27 sludge, enabling the conversion of a waste into a cementitious binder with potentially very
28 high waste loadings, and providing the first detailed nanostructural description of the material
29 thus formed.

30
31 **Keywords:** Magnesium silicate hydrate, Disordered materials, Radioactive waste, Nuclear
32 magnetic resonance, Dispersion,

33

34 1. Introduction

35 The United Kingdom has operated a fleet of Magnox nuclear power plants for over 50 years,
36 utilising natural uranium fuel clad in an Mg-Al alloy (Magnox) casing. Corrosion of this
37 cladding during reprocessing and storage has resulted in the accumulation of a substantial
38 quantity of legacy Mg(OH)₂-rich sludges in storage ponds and silos. In 2013 it was estimated
39 that there were 1497 m³ of sludge in the Magnox Fuel Storage Pond alone,¹ mainly
40 constituting Mg(OH)₂ with some corroded uranium, hydrotalcite
41 (Mg₆Al₂(CO₃)(OH)₁₆·4H₂O),² and artinite (Mg₂CO₃(OH)₂·3H₂O),³ along with a significant
42 quantity of mixed radionuclides including ⁹⁰Sr, ¹³⁷Cs, ²⁴¹Am and isotopes of Pu.⁴ In the UK
43 these sludges are classified as Intermediate Level Wastes (ILW), that is, significantly
44 radioactive but not heat generating,² and thus treatment is required for their safe
45 immobilisation and disposal.

46

47 Portland Cement (PC) composites blended with high quantities of supplementary
48 cementitious materials such as blast furnace slag (BFS) and fly ash (FA) have long been the
49 preferred matrices for the encapsulation of much of the ILW inventory in the United
50 Kingdom⁵. A recent study by Collier and Milestone⁶ reported that no significant chemical
51 interaction occurred between Mg(OH)₂ sludge and FA:PC and BFS:PC cement matrices, with
52 no identifiable incorporation of magnesium into the hydrated binder products. This indicated
53 that the solids of the sludge were encapsulated in the matrix, rather than chemically bound.
54 The use of PC-based materials may not be optimal for Magnox sludge
55 immobilisation/encapsulation as the variable water content of the sludges can cause issues
56 related to the release of bleed water when blended with conventional encapsulation grouts.⁷
57 The conventional PC-based grouts also occupy a significant space as a matrix to encapsulate
58 the waste, limiting the physical space for waste loading possible per package. The
59 development of a tailored binder, which uses the sludge as the basis for a cementitious

60 matrix, could enable higher waste loadings to be achieved, and could also reduce the footprint
61 of the encapsulated waste in a future geological disposal facility (GDF).

62

63 Alternative binders such as magnesium-based cements have been studied in recent years as
64 part of the push towards reducing the environmental footprint associated with the production
65 of Portland cement materials, and the development of sustainable fit-for purpose alternative
66 cements.⁸ This largely stems from the ability to calcine magnesite (MgCO_3) to form magnesia
67 (MgO) at a lower temperature than is required for the conversion of calcite (CaCO_3) to PC,
68 leading to potential energy savings.⁹ Magnesium-based cements are often produced by
69 combining MgO with phosphates or magnesium chlorides, to form magnesium phosphate
70 cements (also known as chemically bonded phosphate ceramics or acid-base cements)¹⁰ or
71 magnesium oxychloride cement,¹¹ respectively. However, in the last decade magnesium
72 silicate hydrate (M-S-H) cements based on blends of MgO and silica fume have attracted
73 attention as binders in refractory castables, and as lower pH cements for the immobilisation
74 of ILW containing reactive metals, which would corrode and generate hydrogen if
75 encapsulated in PC-based materials.¹²

76

77 The $\text{MgO-SiO}_2\text{-H}_2\text{O}$ system has been the subject of studies to determine the reaction products
78 formed from solution, both under hydrothermal¹³ and low temperature¹⁴ conditions, with a
79 combination of both talc and serpentine-like phases identified among the reaction products.
80 Studies have increasingly focussed on the potential for M-S-H as a cement, using dead burnt
81 $\text{MgO-silica fume (SF)}$ blends at ambient temperatures,¹⁵ light burnt MgO-SF blends,^{12a} and
82 $\text{MgO-MgCO}_3\text{-SF-quartz sand}$ composites.^{12c} However, work based on the use of Mg(OH)_2 as
83 the main Mg source has not been as prominent, and the formation of M-S-H type gels within
84 the $\text{Mg(OH)}_2\text{-SF-H}_2\text{O}$ system cured at near-ambient temperatures has not been studied for
85 cementing applications.

86

87 The formation of poorly crystalline M-S-H gels has also been identified in conventional
88 Portland cements after exposure to sulfate attack,¹⁶ and it has been postulated that M-S-H
89 forms as a secondary product in BFS:PC blended cements.¹⁷ Recent studies have also
90 identified M-S-H as an alkaline-alteration product of nuclear waste glasses,¹⁸ and as a phase
91 formed in low-pH cements as a result of interactions with groundwater under nuclear waste
92 repository conditions.¹⁹ The identification of such phases in these key environments related to
93 nuclear waste disposal highlights the importance of developing a full structural
94 characterisation of the M-S-H gel, which remains poorly understood at present.

95

96 In this study hydrated $\text{Mg}(\text{OH})_2$:SF blends are produced and characterised up to 28 days of
97 curing, with a focus on assessing workability, strength, phase development and gel structure
98 of the M-S-H system. Due to industry and regulatory concerns about the possibility of
99 organic superplasticisers enhancing radionuclide solubility within nuclear wasteform
100 cements,²⁰ the application of an inorganic deflocculant (sodium hexametaphosphate
101 $(\text{NaPO}_3)_6$), as used in castables and for clay dispersions²¹ was also investigated as a means to
102 reduce water demand. This additive has previously been used in M-S-H cements,^{12a, 15a} but its
103 effect on fluidity and phase formation within these cements has not yet been described in
104 detail.

105

106

107

108 **2. Experimental methodology**

109 **2.1 Materials**

110 The raw materials used were $\text{Mg}(\text{OH})_2$ from Intermag Company Ltd (<95% purity), silica
111 fume (SF) 181 (Microsilica 940-U, >90% SiO_2) supplied by Elkem as an undensified dry

112 powder, and sodium hexametaphosphate ((NaPO₃)₆, 65-70% P₂O₅ basis) supplied by Sigma-
113 Aldrich.

114

115 **2.2 Formulation design**

116 Throughout the experiments, a mix design of 1:1 Mg(OH)₂:SF was utilised. The influence of
117 the (NaPO₃)₆ in the range 0 to 5 wt.% of the binder, and the water/binder (w/b) ratio, on the
118 workability of the M-S-H system was investigated via mini-slump testing, as described in
119 section 2.4. An initial w/b ratio of 1.2 (defined on a mass basis) was tested at different
120 (NaPO₃)₆ levels, and then this was systematically reduced by 0.1 unit increments until the
121 samples were no longer fluid (i.e. a mini-slump value of 11.3 cm², corresponding to the base
122 area of the cone), to identify the lowest w/b ratio at which the samples could reasonably be
123 mixed and emplaced. For the system without (NaPO₃)₆ the w/b ratio was also increased
124 systematically by 0.1 unit increments from 1.2 due to the low mini-slump values recorded,
125 until a value of ~80 cm² was achieved. Once an optimal level of phosphate addition was
126 identified, the structural development of this paste was then studied over the time of curing.

127

128 **2.3 Mix methodology**

129 To prepare pastes, (NaPO₃)₆ was fully dissolved in distilled water, then Mg(OH)₂ was
130 gradually added over 1 minute, and this suspension was mechanically mixed for 3 minutes
131 before adding the silica fume. Mixing continued for an additional 5 minutes, and pastes were
132 then poured into 50 mL centrifuge tubes, sealed, placed in an environmental chamber at 40
133 °C and 95% relative humidity, and cured for up to 28 days. Preliminary studies showed slow
134 reaction at 20 °C, and therefore an elevated curing temperature of 40 °C was selected.

135

136 **2.4 Analytical methods**

137 Mini-slump testing was performed using a poly(tetrafluoroethene) mini-slump cone
138 (downscaled Abrams cone geometry: 19 mm top diameter, 38 mm bottom diameter, 57 mm
139 height ²²) on a sheet of poly(methyl methacrylate) marked with grid squares of 2 × 2 cm.
140 Freshly mixed pastes were used in triplicate tests, and in each instance a photograph was
141 taken of the final slump from above, from which the slump area was calculated using ImageJ
142 software ²³ calibrated to the grid.

143

144 For compressive strength testing, the paste was poured into 50 mm steel cube moulds,
145 compacted with the use of a vibrating table, sealed and cured as described above. Cubes were
146 demoulded after 3 days and returned to the environmental chamber. Testing was performed in
147 duplicate using a CONTROLS Autamax 5 instrument at a loading rate of 0.25 MPa/s.

148

149 Hardened samples which had been cured for 7, 14 and 28 days were crushed and immersed in
150 acetone for 2 days to arrest hydration, then dried in a vacuum desiccator for a further 2 days.
151 These were then ground with an agate mortar and sieved to <63 μm using a brass sieve for
152 analysis by the following apparatus.

153

154 X-ray diffraction (XRD) was carried out using a STOE STADI P diffractometer (Cu K α ,
155 1.5418 Å) using an imaging plate detector (IP-PSD) to collect data between 10° < 2 θ ≤ 70°,
156 and angle-corrected using a silicon standard. Selected samples were analysed via
157 thermogravimetric analysis (TGA) using a Pyris 1 TGA and differential thermal analysis
158 (DTA) using a Perkin Elmer DTA 7, both using an alumina crucible, at a heating rate of 10
159 °C/min up to 1000 °C in a nitrogen atmosphere. FTIR spectroscopy was undertaken using a
160 Perkin Elmer Spectrum 2000 spectrometer in mid-IR mode using pressed KBr discs
161 containing 2 wt.% powdered sample. Solid state ²⁹Si NMR spectra were collected on a Varian

162 VNMRs 400 (9.4 T) using a 6 mm o.d. zirconia rotor. Chemical shifts were externally
163 referenced to tetramethylsilane (TMS) at 0 ppm. ^{29}Si MAS NMR spectra for M-S-H were
164 collected at 79.435 MHz, with a spinning speed of 6.8 kHz, a pulse duration of 6.2 μs (90°)
165 and a relaxation time of 30 s, for a minimum of 2000 scans. M-S-H samples for NMR
166 analysis were produced using analytical grade $\text{Mg}(\text{OH})_2$ (Alfa Aesar, 95-100% purity) to
167 eliminate any possibility of Fe contamination. ^{29}Si MAS NMR spectra for mineral samples
168 (lizardite and antigorite) were collected at 79.438 MHz, with a spinning speed of 6 kHz, a
169 pulse duration of 4.5 μs (90°) and relaxation time of 1 s for 43200 scans.

170

171 ^{25}Mg MAS NMR spectra were obtained on a Bruker Advance III 850 spectrometer (19.96 T),
172 using a 4 mm zirconia rotor, with a spinning speed of 10 kHz (M-S-H, lizardite and talc) and
173 14 kHz (antigorite – required due to signal broadening from iron). Spectra were collected at
174 52.05 MHz with a pulse duration of 5 μs (90°) and relaxation time of 2 s. Higher iron
175 contents in these two samples enabled a faster relaxation time to be used than with the M-S-H
176 materials. Chemical shifts were externally referenced to either MgO (26 ppm) or a 1 M
177 MgCl_2 (0 ppm) solution.

178

179 **3. Results and discussion**

180 **3.1 Influence of $(\text{NaPO}_3)_6$ addition**

181 **3.1.1. Mini-slump**

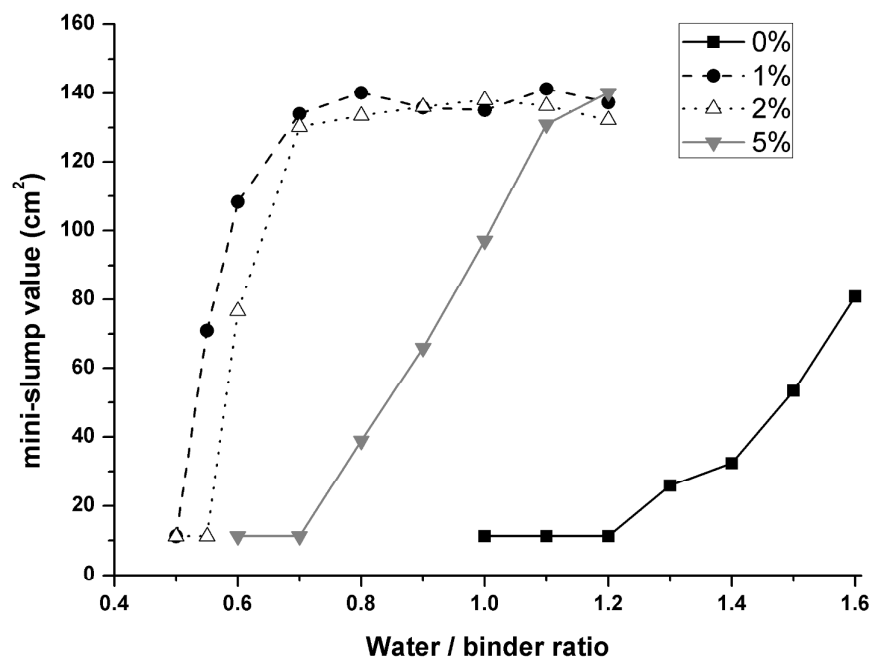
182 The addition of $(\text{NaPO}_3)_6$ as an inorganic dispersant led to vast differences in the workability
183 between the samples produced, as shown in Figure 1. With no phosphate addition, the paste
184 was thick and lacked fluidity, and a w/b ratio as high as 1.6 was required to achieve a
185 minislump of $\sim 80\text{ cm}^2$. For comparison, using a mini-slump test in this geometry, a typical

186 Portland cement paste with a w/b ratio of 0.36 and no organic admixtures achieved 27 cm^2 ,
 187 and with a w/b ratio of 0.5 achieved 68 cm^2 .²²

188

189 The addition of 1 wt.% $\text{Na}(\text{PO}_3)_6$ consistently produced a higher fluidity than the other
 190 formulations, though only marginally more than the 2 wt.% formulation. Both 1 and 2 wt.%
 191 enabled retention of a high fluidity, $\sim 130 \text{ cm}^2$, down to w/b = 0.7, with zero slump only
 192 reached at w/b = 0.50 using 1 wt.% $\text{Na}(\text{PO}_3)_6$, and w/b = 0.55 using 2 wt.%. Some loss of
 193 fluidity was observed at 5 wt.% (NaPO_3)₆ addition, with higher w/b ratios required in order to
 194 achieve similar mini-slump values compared to the formulations with 1 and 2 wt.%
 195 (NaPO_3)₆. This indicates that a threshold limit exists, beyond which the dispersion is no
 196 longer as effective, when too much phosphate is added.

197



198

199 **Figure 1.** Mini-slump values for 1:1 $\text{Mg}(\text{OH})_2:\text{SiO}_2$ with 0-5 wt.% (NaPO_3)₆ as shown in the
 200 legend, as a function of water/binder ratio. A measurement of 11.3 cm^2 indicates no slump, as

201

this is the initial slump cone area

202

203 The ability to maintain a high workability over a wide range of w/b ratios by using $(\text{NaPO}_3)_6$
204 as a dispersant enables a wider range of sludges to be used as a feedstock, due to their
205 variable water content. Correspondingly, significantly less water is required to fluidise the
206 system, compared to the phosphate free system. This is important, as the w/b ratio has a key
207 impact on porosity in cementitious systems, and reducing water content is the most
208 straightforward way to lower the porosity of the hardened material. Porosity of a cementitious
209 binder is intrinsically linked to permeability, and consequently plays a major role in
210 determining the mobility of radionuclides in the long-term leaching of cementitious
211 wastefoms.²⁴

212

213 3.1.2. Compressive strength

214

215 In the hardened state, the physical effects of changing the dose of $(\text{NaPO}_3)_6$ had only minor
216 effects for a given w/b ratio. Figure 2 shows the development of compressive strength as a
217 function of curing duration for samples with a w/b ratio of 1.0. All samples exhibited slow
218 strength gain during the first 28 days, with the samples containing any amount of $(\text{NaPO}_3)_6$
219 producing similar compressive strengths at each age of curing. The low strengths shown here
220 are related to the high water/binder ratio of this sample set, which prevents the development
221 of a strong microstructure. The sample formed in the absence of $(\text{NaPO}_3)_6$ produced the
222 lowest strength after 28 days. This is likely to be a consequence of the presence of voids and
223 bubbles within the samples caused by the extremely viscous paste produced, which was
224 difficult to cast into the moulds despite the use of a vibrating table.

225

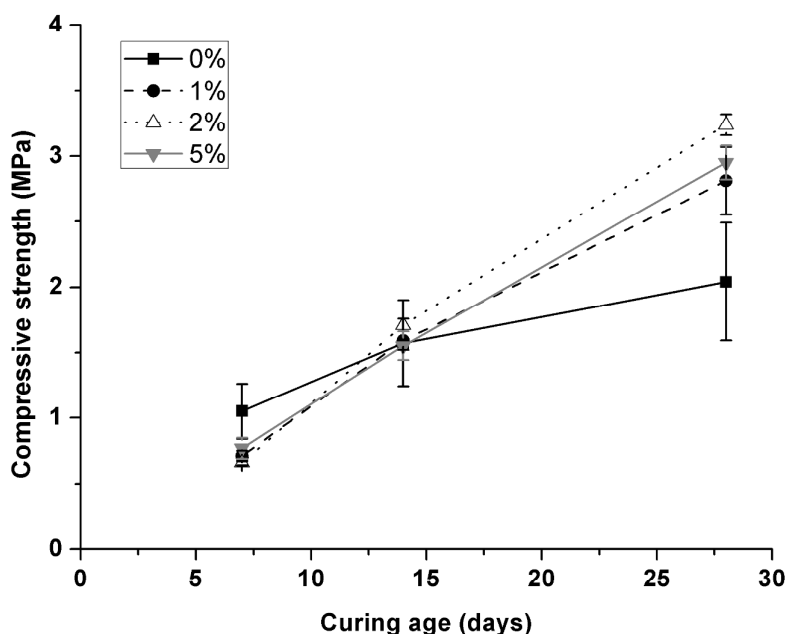


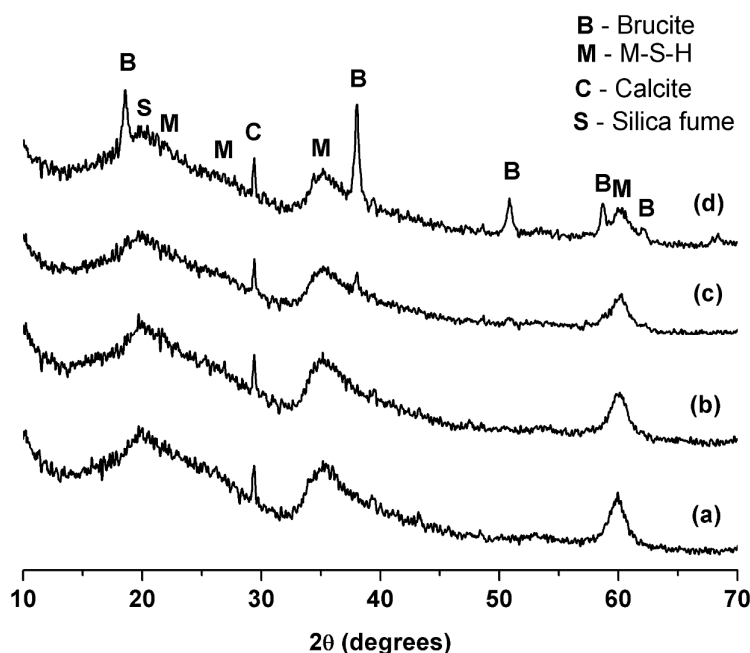
Figure 2. Compressive strength of 1:1 Mg(OH)₂:SiO₂ pastes, w/b = 1.0, with 0–5 wt.% (NaPO₃)₆

All of the samples produced with w/b = 1.0 exhibited lower compressive strengths than is recommended for use in a typical nuclear waste package (4 MPa for a 500 L drum),²⁵ but at 14 and 28 days did exceed the 0.7 MPa which is the baseline performance requirement for material handling. On this basis, and to offer chemical consistency throughout all samples, this w/b ratio was selected for use in characterisation of the hardened binder products.

3.1.2. X-ray diffraction

Figure 3 shows similar hydration products formed in the tested samples, with brucite (Mg(OH)₂, PDF # 74-2220) and silica fume consumed to varying degrees at different levels of phosphate addition, to produce M-S-H. Calcite (CaCO₃, PDF # 05-0586) was identified as a minor impurity in the commercial-grade Mg(OH)₂. In the XRD patterns poorly crystalline

241 M-S-H is clearly observed via diffuse scattering at 20° , 36° and 61° 2θ , with a minor diffuse
 242 reflection at 28° 2θ . These diffractograms are similar to those observed for other M-S-H
 243 systems,^{13b, 15b} as well as for mechanically amorphised talcs²⁶ and for ground chrysotile;
 244 these phases are both considered potential structural models for M-S-H.²⁷ Excess silica fume
 245 is identified via a diffuse reflection centred at 20° 2θ , partially overlapping one of the M-S-H
 246 reflections. The formation of M-S-H appeared to be retarded when $(\text{NaPO}_3)_6$ was added
 247 beyond 1 wt.%; this was clearly observed in the XRD data for the 2 wt.% and 5 wt.% samples
 248 after 28 days of curing.

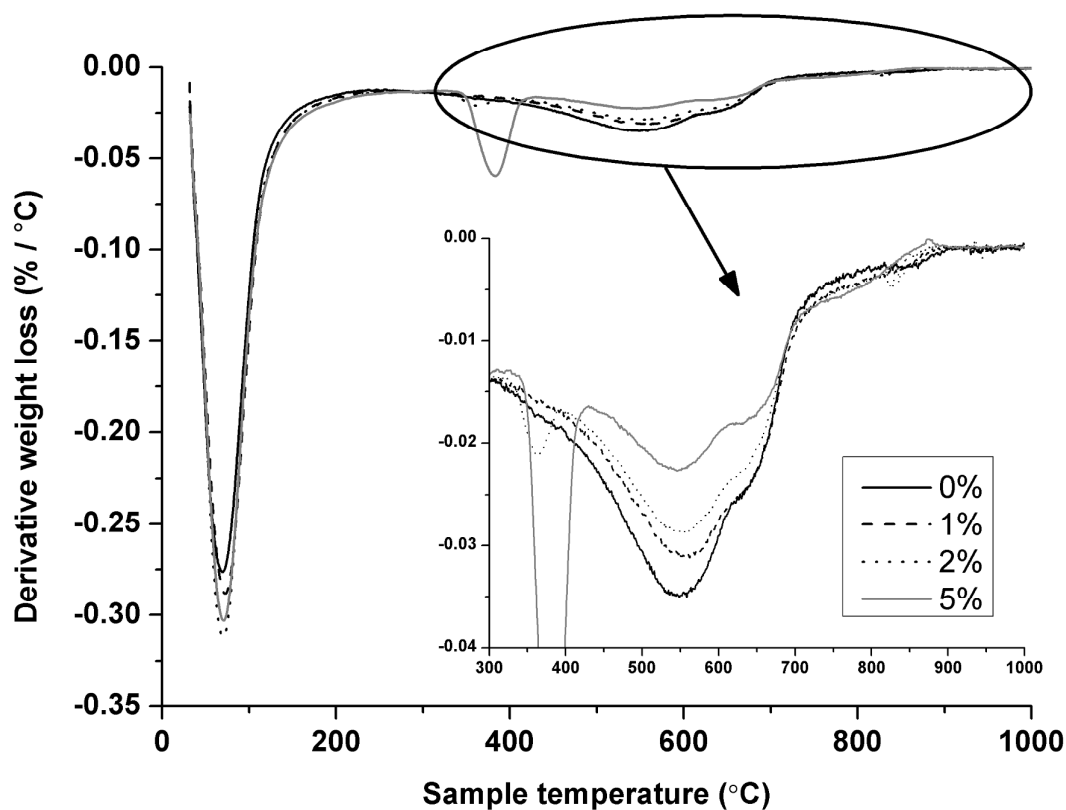


249
 250 **Figure 3.** X-ray diffraction patterns of 28 day-cured 1:1 $\text{Mg}(\text{OH})_2$: SiO_2 ($w/b = 1.0$) binders,
 251 with (a) 0, (b) 1, (c) 2 and (d) 5 wt.% $(\text{NaPO}_3)_6$ addition
 252

253 3.1.3. Thermal analysis

254 The derivative thermogravimetry (DTG) data presented in Figure 4 correlate well with the
 255 diffractograms in Figure 3, recording higher residual contents of $\text{Mg}(\text{OH})_2$ (decomposition
 256 peak at $\sim 400^\circ\text{C}$ ²⁸) in the samples with increasing addition of phosphate. The weight loss at

257 temperatures up to ~ 150 °C is assigned to the release of adsorbed water from the surface of
 258 the M-S-H,^{13c} as well as free water held in the pores of the hardened gel. Any crystalline talc
 259 present would lose structural water at 875 - 1000 °C,²⁸ and thus is identifiably absent from
 260 these samples (consistent with the XRD data), while poorly crystalline talcs, ground
 261 chrysotile, ground antigorite and M-S-H are known to lose water slowly over a wide
 262 temperature range below 700 °C.^{13b, c, 14b, 27, 29}



263

264 **Figure 4.** DTG data for 1:1 Mg(OH)₂:SiO₂ (w/b = 1.0) with 0 – 5 wt.% (NaPO₃)₆, samples
 265 cured for 28 days. Inset shows the data above 300 °C with an expanded vertical scale

266

267 Table 1 shows a quantitative breakdown of the thermogravimetric data in key temperature
 268 regions of interest, for samples cured for different durations. The mass loss between 340 –
 269 440 °C represents the quantity of unreacted Mg(OH)₂, and it is evident that even at 1 wt.%

270 addition of $(\text{NaPO}_3)_6$, the rate of $\text{Mg}(\text{OH})_2$ consumption was reduced compared to the
 271 phosphate-free sample. More unreacted $\text{Mg}(\text{OH})_2$ was present after 7 and 14 days of curing
 272 in the presence of phosphate, although for 1 and 2 wt.% $(\text{NaPO}_3)_6$, parity with the phosphate-
 273 free system was reached after 28 days. Addition of 5 wt.% phosphate reduces $\text{Mg}(\text{OH})_2$
 274 consumption at all ages studied, which is consistent with the XRD analysis in section 3.1.2;
 275 the mass loss peak is much more prominent in this sample than in the others shown in Figure
 276 4.

277

278 **Table 1.** Mass loss (%) determined by TGA in different temperature ranges for 1:1
 279 $\text{Mg}(\text{OH})_2:\text{SiO}_2$ (w/b = 1.0) with 0 – 5 wt. % $(\text{NaPO}_3)_6$, at different curing durations.

280

Uncertainty in calculated mass loss approx. $\pm 0.2\%$

		Mass loss (%)		
Temperature range (°C)	Na $(\text{PO}_3)_6$ (wt. %)	Curing duration (days)		
		7	14	28
25 to 1000	0	27.2	27.9	29.2
	1	27.2	28.0	29.8
	2	26.1	27.4	30.1
	5	26.0	27.2	30.2
340 to 440	0	7.2	3.6	2.3
	1	10.2	5.5	2.2
	2	11.1	6.6	2.3
	5	10.6	7.6	4.1
450 to 1000	0	5.8	7.0	7.4
	1	5.4	6.2	7.0
	2	4.9	5.8	6.5
	5	4.2	4.8	5.4

281

282 In Figure 4, the region between 450 and 700 °C was seen to consist of two peaks, located at
 283 550 °C and 640 °C. The peak at 550 °C is identified as being due specifically to M-S-H
 284 decomposition, with the peak at 640 °C assigned to the decomposition of calcite (CaCO_3),³⁰

285 which is introduced into each sample in equal proportions as an impurity in the $\text{Mg}(\text{OH})_2$. As
286 previously mentioned, the M-S-H loses water slowly and over a very wide temperature range,
287 and thus, the mass loss event at 450–1000 °C is treated as characteristic for its analysis in
288 Table 1, assuming a constant CaCO_3 contribution in all samples.

289

290 Magnesite (MgCO_3) decomposes at 527-615 °C,³⁰⁻³¹ but this phase was not identified by
291 FTIR or XRD analysis, and so is not considered to contribute significantly to the DTG
292 profile. Other (hydrous) magnesium carbonates would show distinctive low-temperature
293 decomposition peaks, and also were not identified by XRD or FTIR.

294

295 The inset in Figure 4 demonstrates a clear difference between the samples at 28 days of age,
296 which is also quantified in Table 1 for each curing age. If it was assumed that M-S-H was
297 structurally similar between the samples, this would indicate that M-S-H formation increased
298 with curing age, and was retarded by the phosphate additions. This is in agreement with the
299 differences observed in the diffraction patterns (Fig. 3). However, when comparing between
300 the 0 and 1 wt.% $(\text{NaPO}_3)_6$ data, the mass loss in Table 1, for $\text{Mg}(\text{OH})_2$ decomposition (340-
301 440 °C) remains the same (and XRD analysis (Fig. 4) suggests complete $\text{Mg}(\text{OH})_2$
302 consumption), however the mass loss for M-S-H is different between these two. This
303 suggests there might be a structural difference in the M-S-H gels forming due to the effect of
304 the phosphate additive.

305

306

307 **3.2. Structural evolution**

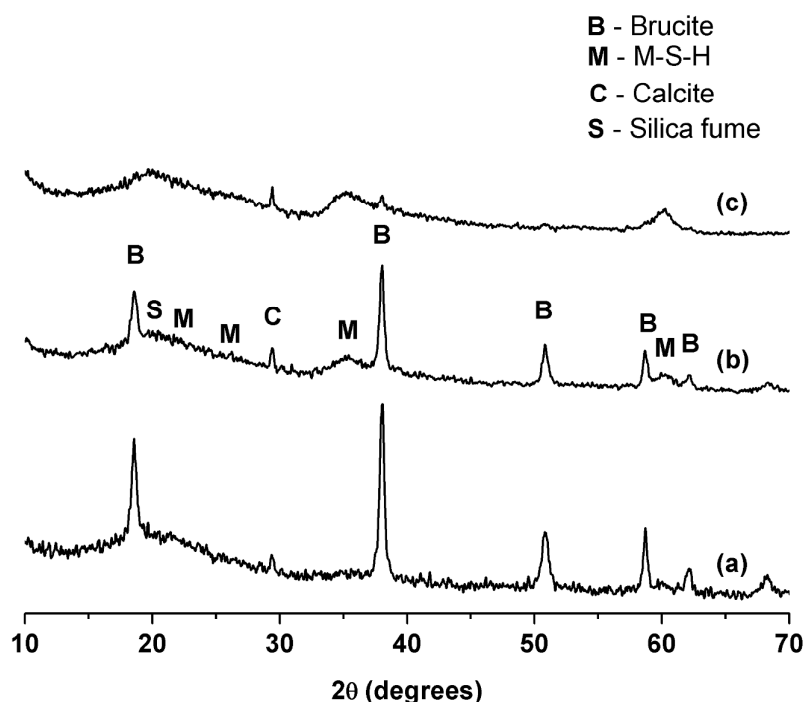
308

309 **3.2.1. X-ray diffraction and thermal analysis**

310

311 Based on the discussion in the preceding section, further analysis was undertaken to
 312 understand the structural evolution of a phosphate modified system. A 1:1 $\text{Mg}(\text{OH})_2:\text{SiO}_2$
 313 blend, using a w/b ratio of 1.0 and 2 wt. % $(\text{NaPO}_3)_6$, was used as it developed the highest
 314 compressive strength among the samples tested at this w/b ratio.

315



316

317 **Figure 5.** X-ray diffractograms of 1:1 $\text{Mg}(\text{OH})_2:\text{SiO}_2$ (w/b = 1.0) with 2 wt.% $(\text{NaPO}_3)_6$ at
 318 curing ages of (a) 7, (b) 14 and (c) 28 days

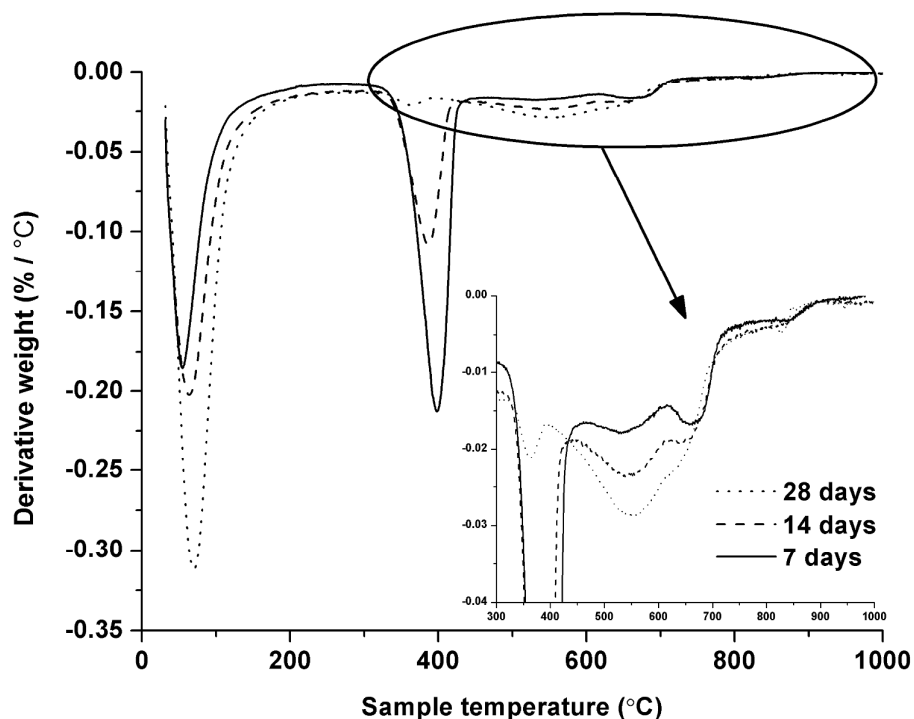
319

320 The structural development of the binder can be seen in the diffractograms in Figure 5, where
 321 decreasing intensity of the brucite ($\text{Mg}(\text{OH})_2$) reflections is evident, along with increasing
 322 intensity of M-S-H reflections as the curing process progresses. This correlates well with the
 323 DTG data for samples with different curing durations (Fig. 6), demonstrating that longer-term
 324 curing led to lower mass loss at $\sim 400^\circ\text{C}$ ($\text{Mg}(\text{OH})_2$ decomposition), and larger mass losses in
 325 the regions 25 - 150 $^\circ\text{C}$ and $\sim 550^\circ\text{C}$, both of which can be used as indicators of M-S-H

326 formation. As in Figure 4, these DTG data also show a double peak in the region 450-700 °C.
 327 At early ages both peaks appear to have a similar intensity, but the peak at 550 °C increases
 328 at later curing ages, while that for the calcite decomposition at 650 °C remains constant.

329

330



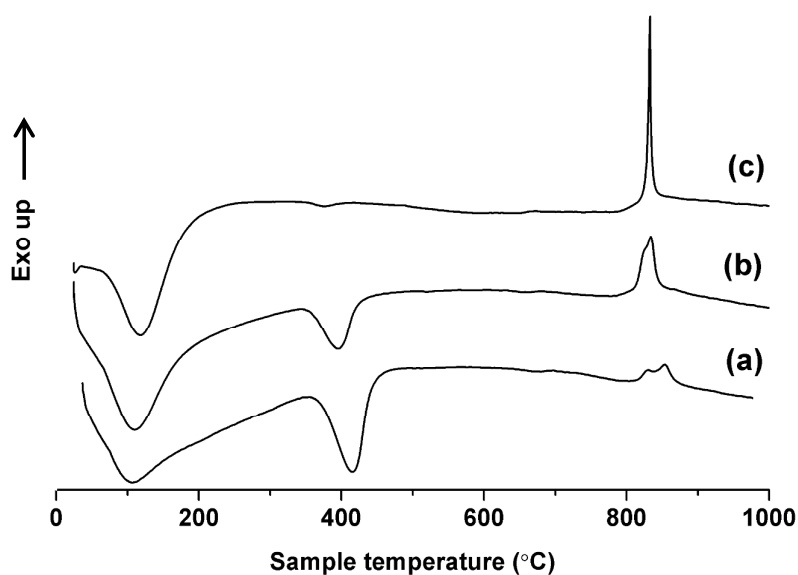
331

332 **Figure 6.** DTG data for 1:1 Mg(OH)₂:SiO₂ (w/b = 1.0) with 2 wt.% (NaPO₃)₆, at curing ages
 333 of 7, 14 and 28 days

334

335 The DTA data for the M-S-H binder (Fig. 7) show endothermic heat flow features in similar
 336 temperature ranges to those observed as mass loss peaks in DTG, but with an additional
 337 exotherm at 800-850 °C, which becomes sharper and more intense with greater sample
 338 maturity. This signal changes from two shallow exotherms (826 and 853 °C) after 7 days, to
 339 one strong sharp exotherm at 833 °C after 28 days. This change is not associated with a mass
 340 loss event in the DTG data, and therefore has been identified as the crystallisation of M-S-

341 H.^{13b, 14b} Similar crystallisation events have been observed in thermal treatment of
342 amorphised talc,^{29a} which is converted to enstatite (MgSiO_3) at this temperature.²⁶
343 Comparable exotherms are noted in natural serpentine minerals, with chrysotile exhibiting a
344 particularly sharp exotherm, forming a mixture of enstatite and forsterite (Mg_2SiO_4) upon
345 heating.³²
346

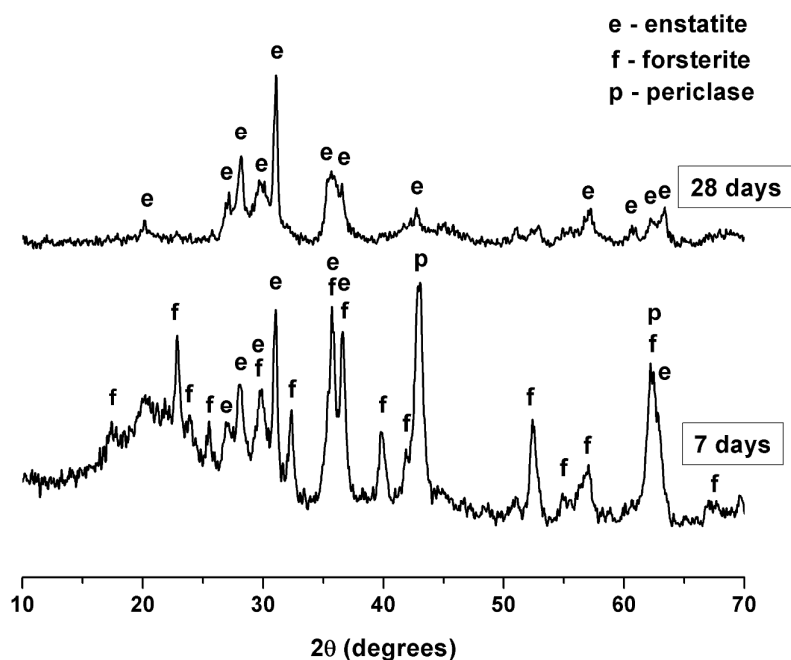


347
348 **Figure 7.** DTA data for 1:1 $\text{Mg}(\text{OH})_2:\text{SiO}_2$ (w/b = 1.0) with 2 wt.% $(\text{NaPO}_3)_6$, at curing ages
349 of (a) 7, (b) 14 and (c) 28 days

350
351 To further understand the exotherms observed in the DTA data, samples cured for 7 and 28
352 days were heated to 900 °C and analysed by XRD to determine the crystalline phases formed
353 (Fig. 8). There is a clear difference observed between the samples. For the 28 day cured
354 sample, only enstatite (MgSiO_3 , PDF # 73-1758) was present, similar to the thermal treatment
355 of amorphised talc as noted above. On the other hand, for the 7 day cured sample, in addition

356 to enstatite, forsterite (Mg_2SiO_4 , PDF # 34-189), periclase (MgO , PDF # 89-4248) and a
357 broad band around $\sim 22^\circ 2\theta$ assigned to low-crystallinity silica were also observed.

358



359

360 **Figure 8.** XRD patterns of 1:1 $\text{Mg}(\text{OH})_2:\text{SiO}_2$ ($w/b = 1.0$) heated to 900°C after 7 and 28
361 days of curing

362

363 The presence of a single, sharp exotherm in the DTA data for the 28 day cured M-S-H (Fig.
364 7) can be explained by the presence of only enstatite after heating (Fig. 8). The shallower
365 double peak observed in the DTA data for the 7 day cured sample could be attributed to a less
366 developed and less homogeneous M-S-H gel structure, which crystallised into enstatite and
367 forsterite at slightly different temperatures. The significant amount of periclase in the 7 day
368 cured sample is due to the dehydroxylation of remnant $\text{Mg}(\text{OH})_2$ upon heating.

369

370

371

372

373 **3.2.2. Fourier transform infrared spectroscopy**

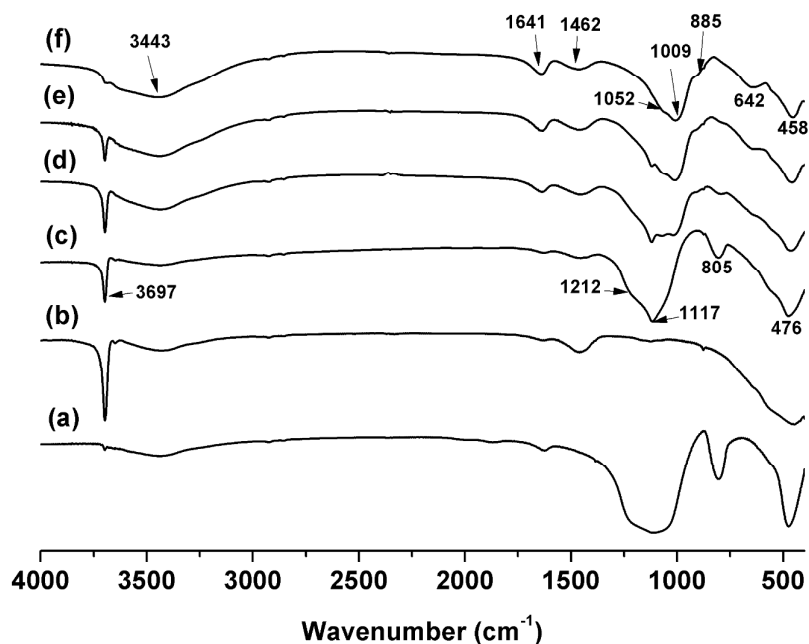
374

375 The FTIR data shown in Figure 9 demonstrate the evolution of phases with time, from the
376 raw materials to the 28 day cured sample. The silica fume used in the present study (Figure
377 9a) had a spectrum similar to that of vitreous silica, with broad bands at 1110 cm^{-1} and 803
378 cm^{-1} arising from Si-O stretching, and at 475 cm^{-1} arising from O-Si-O bending.³³ $\text{Mg}(\text{OH})_2$
379 (Figure 9b) displayed a characteristic OH vibration at 3698 cm^{-1} and libration at 415 cm^{-1} ,
380 with adsorbed water at $\sim 3400\text{ cm}^{-1}$ and the broad carbonate vibration of the calcite impurity
381 at 1450 cm^{-1} .³⁴ The anhydrous mix (Figure 9c) naturally showed the features of these raw
382 materials combined.

383 Upon reaction, some of these features from the raw materials became less prominent (Figures
384 9d,e), and the spectrum of the 28 day sample (Figure 9f) became very similar to those
385 previously reported for other M-S-H gels.^{14a}

386 It is noted that the spectrum of the 28 day curing sample also resembles those for partially
387 amorphised talc,^{26, 29a} ground chrysotile,²⁷ and ground antigorite.^{29b} Libration of the Mg_3OH
388 unit in talc has been observed at 669 cm^{-1} , along with a vibration of chrysotile at 608 cm^{-1}
389 (shoulder at 645 cm^{-1}),³⁵ and similar modes are likely to be causing the peak seen in the M-S-
390 H at 642 cm^{-1} . The Si-O-Si vibrations of the tetrahedral sheets within the talc structure are
391 recorded at 1018 cm^{-1} and 1047 cm^{-1} ,³⁶ while amorphised chrysotile exhibits in-plane Si-O
392 and out-of-plane Si-O stretching at 1025 cm^{-1} and 1082 cm^{-1} respectively, with asymmetric
393 Si-O stretching at 960 cm^{-1} .²⁷ The broad band centred at 1009 cm^{-1} , with a broad shoulder at
394 1052 cm^{-1} , in the M-S-H is likely to be related to similar structural motifs.

395 The broad bands at $\sim 3400\text{ cm}^{-1}$ and 1640 cm^{-1} , which increase in intensity with age, are
396 suggestive of water adsorbed to surfaces or incorporated in disordered reaction products.
397 Some contribution in this region may also be from Si-OH vibrations due to the hydrated
398 residual silica, which may also be producing the shoulder seen at $\sim 885\text{ cm}^{-1}$.



399

400 **Figure 9.** FTIR spectra of (a) silica fume, (b) $\text{Mg}(\text{OH})_2$, (c) 1:1 $\text{Mg}(\text{OH})_2$: SiO_2 with 2 wt.%
401 $(\text{NaPO}_3)_6$ as an anhydrous powder mix, and hydrated samples cured for (d) 7, (e) 14 and (f)
402 28 days (w/b = 1.0 for all hydrated samples)

403

404

405 3.3. Nuclear Magnetic Resonance (NMR) spectroscopy

406

407 ^{29}Si and ^{25}Mg MAS NMR experiments were carried out to identify any structural changes
408 occurring in these binders at advanced times of curing (up to 8 months), and the effect of
409 $(\text{NaPO}_3)_6$ addition on the structure of the M-S-H formed in the 1:1 $\text{Mg}(\text{OH})_2$: SiO_2 binder

410 system. The ^{29}Si NMR spectra of M-S-H samples with 0% and 2% $(\text{NaPO}_3)_6$ after 1 and 8
411 months of curing are reported in Figure 10.

412

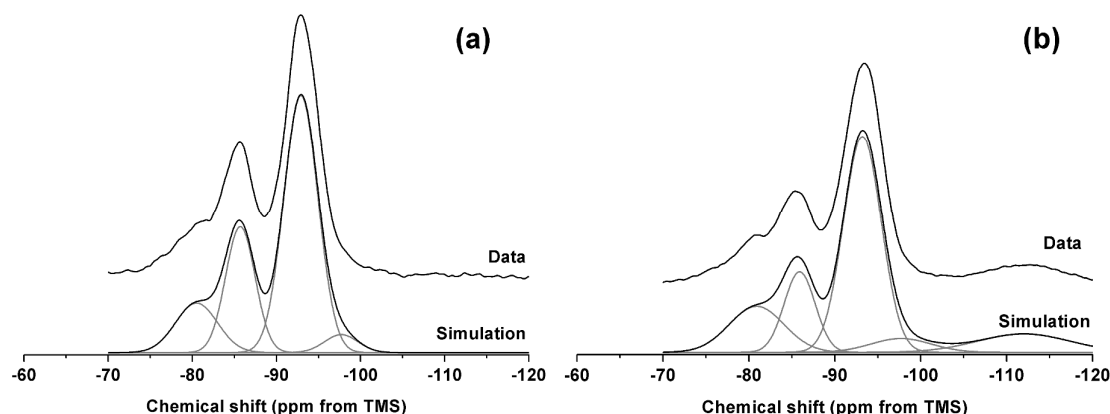
413 The ^{29}Si MAS NMR spectra in Figure 10 are in good agreement with previously reported
414 spectra for synthetic M-S-H type gels produced using MgO as the main Mg source.^{14b, 15a, 37}

415 Both the 1 and 8 month data sets resemble most closely the aged (6 months) high-Mg
416 samples produced at 85 °C by Brew and Glasser,^{14a} and the peak assignments presented here
417 follow the general trends identified by those authors.

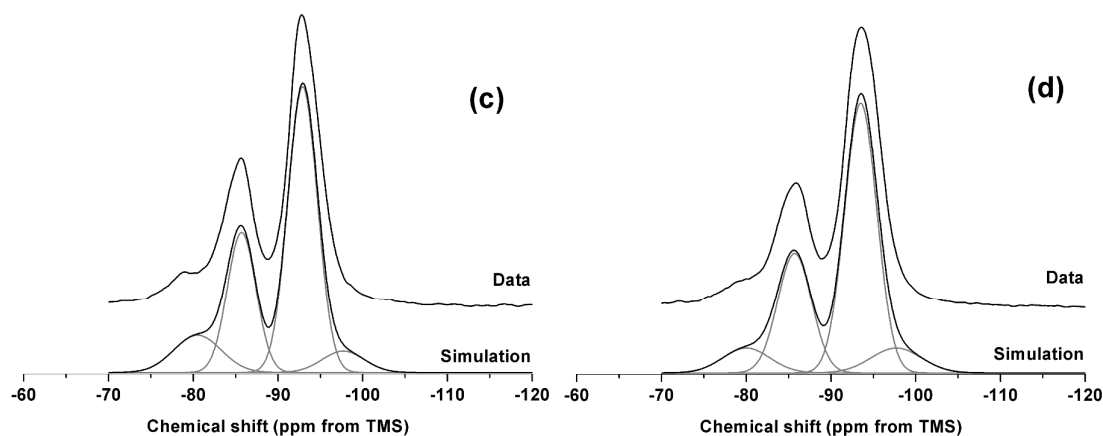
418

419 Deconvolution of the spectra enabled the identification of five peaks, with very minor shifts
420 between spectra (Table 2). For the two spectra obtained after 1 month of curing, Q^1 and Q^2
421 peaks centred at around -81 and -86 ppm respectively were identified, with the Q^3 region split
422 between two peaks centred at (a) -93 and (b) -97.7 ppm, respectively. It is noted that the ^{29}Si
423 MAS NMR spectra of serpentine minerals and talc typically exhibit peaks in the Q^3 region,
424 while broader Q^1 and Q^2 bands signify a less structured gel. The major Q^3 (a) peak at -93 ppm
425 was consistent with the Q^3 resonance typically identified in both chrysotile³⁸ and antigorite,³⁹
426 while the smaller Q^3 (b) peak at -97.7 ppm was assigned to a Q^3 site environment similar to
427 those typically present in talc.²⁸

428



429



430

431 **Figure 10.** ^{29}Si MAS NMR spectra for 1:1 $\text{Mg}(\text{OH})_2:\text{SiO}_2$ (w/b 1.0) with (a) 0 and (b) 2 wt.
 432 % $(\text{NaPO}_3)_6$ at a curing age of 1 month, (c) 0 and (d) 2 wt. % $(\text{NaPO}_3)_6$ after 8 months of
 433 curing. The data presented include a simulation and constituent peaks underneath.

434

435 **Table 2.** Peak positions and widths (ppm) for deconvolutions shown in Figure 10. Estimated
 436 uncertainty in calculated intensities $\pm 1\%$

$(\text{NaPO}_3)_6$		1 month					8 months			
		Q^1	Q^2	$\text{Q}^3(\text{a})$	$\text{Q}^3(\text{b})$	Q^4	Q^1	Q^2	$\text{Q}^3(\text{a})$	$\text{Q}^3(\text{b})$
0 wt. %	Centre	-80.5	-85.7	-92.9	-97.7	-	-80.5	-85.7	-92.9	-97.7
	FWHM	5.9	4.1	4.8	4.7	-	6.6	4.0	4.1	5.9
	Intensity (%)	13.7	24.4	57.9	4.0	-	11.6	26.5	55.9	6.0
2 wt. %	Centre	-80.9	-85.9	-93.2	-97.7	-112	-80.0	-85.7	-93.5	-97.7
	FWHM	7.5	4.2	5.2	8.2	12.7	6.6	4.7	4.5	7.1
	Intensity (%)	16.1	15.8	52.1	5.3	10.7	7.7	26.6	57.3	8.3

437

438

439 The relatively high $\text{Q}^3(\text{a+b})/\text{Q}^2$ intensity ratio in Figure 10 is indicative of a high level of
 440 structural development in the gel. The addition of 2 wt.% $(\text{NaPO}_3)_6$ leads to the presence of a
 441 peak centred at -112 ppm after 1 month, attributed to Q^4 species in unreacted silica fume⁴⁰

442 and indicating a lower extent of reaction, resulting in lower intensity Q^3 and Q^2 peaks. This
443 indicates that with no addition of $(NaPO_3)_6$ the silica fume had completely reacted, while the
444 presence of phosphate had retarded the conversion of silica fume to M-S-H.

445

446 After 8 months of curing, the spectra had changed slightly compared with those observed in
447 the specimens after 1 month of curing. There was a decrease in the Q^1 region for both 0 and 2
448 wt. % phosphate samples, which suggests that further structural development of M-S-H
449 occurred in the samples, leading towards the formation of a more cross-linked structure. After
450 8 months of curing the resonance assigned to the Q^4 sites of unreacted silica fume was no
451 longer present in the phosphate-containing sample, indicating that the silica fume in these
452 binders has been fully consumed at this time.

453

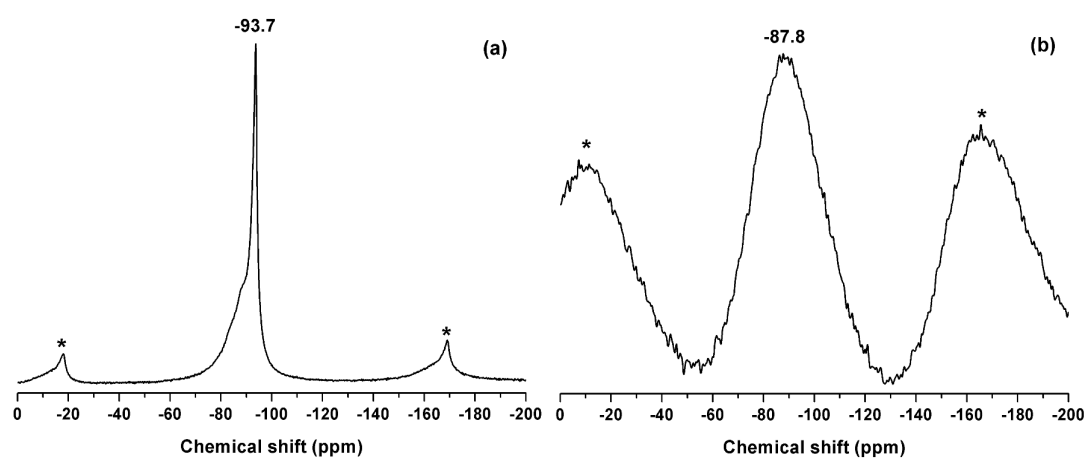
454 The structure of M-S-H has previously been proposed to resemble a poorly crystalline talc-
455 like material.^{13a} Talc typically exhibits a single ^{29}Si peak at -97.7 ppm,²⁸ however this peak
456 was only a minor Q^3 component within the binders produced in this study. The major Q^3
457 component was identified at -93 ppm, which corresponds to that typically found in the
458 serpentine group of minerals (polymorphs of $Mg_3(Si_2O_5)(OH)_4$, such as chrysotile, lizardite
459 and antigorite). The reported ^{29}Si NMR peak locations for these minerals vary slightly from
460 publication to publication, potentially due to the slight variations in chemical composition of
461 each natural sample due to Fe, Ca and Al inclusions. Both chrysotile³⁸ and antigorite^{39b} have
462 reported values close to -93 ppm, although the antigorite spectrum is broad, while data for
463 lizardite are difficult to obtain.

464

465 To clarify the details of the M-S-H structure formed here, natural mineral samples of lizardite
466 and antigorite were obtained and analysed via ^{29}Si and ^{25}Mg MAS NMR. These samples

467 contained traces of iron (7.0 wt.% in antigorite, 3.4 wt.% in lizardite, on an oxide basis as
468 determined by X-ray fluorescence), broadening the signal and affecting the relaxation times.
469 This was more severe for the antigorite sample. The lizardite was also slightly aluminous (7.1
470 wt.% Al_2O_3), as Al often substitutes for Si in natural samples.⁴¹ These spectra are shown in
471 Figure 11, both exhibiting strong signals within the Q^3 region at around -90 ppm. The broad
472 antigorite spectral feature at -87.8 ppm is downfield of the principal Q^3 peaks in the M-S-H,
473 although the spectrum is not of high resolution, whereas the main lizardite peak at -93.7 ppm
474 matches very closely to the $\text{Q}^3(\text{a})$ site observed within the M-S-H samples. There does exist a
475 broad feature downfield of this peak, which significantly reduces in area when cross polarised
476 with ^1H , suggesting that these environments may resemble less ordered, less hydrated
477 lizardite-like assemblages than the primary $\text{Q}^3(\text{a})$ site.

478



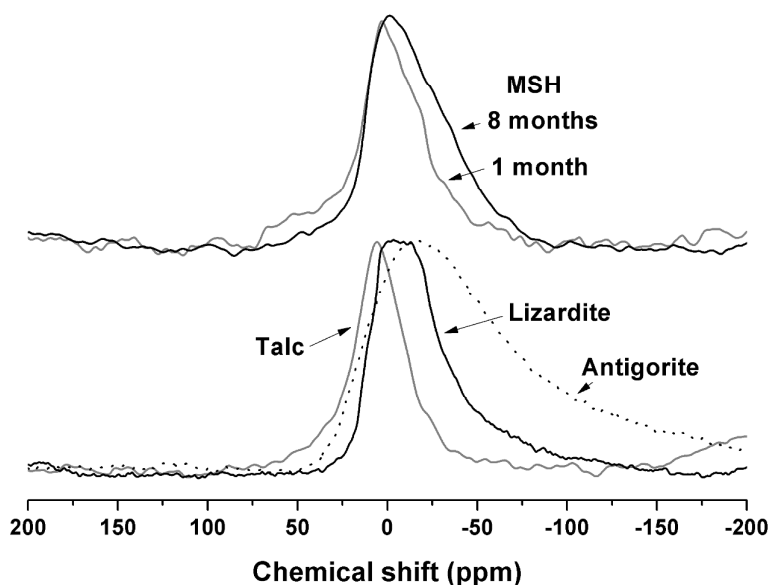
479

480 **Figure 11.** ^{29}Si MAS NMR spectra for: (a) lizardite, (b) antigorite. Spinning sidebands
481 marked with *

482

483 ^{25}Mg MAS NMR data are significantly more difficult to obtain and interpret than is the case
484 for ^{29}Si . The low natural abundance (10%) and low resonance frequency of ^{25}Mg often
485 necessitate the use of very high field instruments (e.g. 20 T used here)⁴². Combined with its

486 quadrupolar nature (spin $5/2$), this makes the interpretation of spectra complex, although
487 recent advances in this field are shedding more light on this less well studied nucleus⁴²⁻⁴³.
488 ^{25}Mg MAS NMR spectra of lizardite, antigorite and talc are overlaid with the spectra of 1 and
489 8 month cured M-S-H samples (with 0% $(\text{Na}_3\text{PO}_4)_6$) in Figure 12. A clear change in
490 lineshape is observed in the M-S-H samples as curing progresses, with the spectrum shifting
491 upfield. The 8 month M-S-H sample specifically aligns well with the lizardite spectrum (as
492 compared in Fig. 13), compared to the antigorite or talc spectra. It should be noted that being
493 a natural sample, the lizardite contains an impurity of ~ 12 wt.% $\text{Mg}(\text{OH})_2$, which will modify
494 the ^{25}Mg spectrum. At this field strength, second-order quadrupolar interactions of the central
495 transition cause $\text{Mg}(\text{OH})_2$ to exhibit a split double peak from its single Mg site⁴⁴. This double
496 peak is centred -9 ppm, which is in the central part of the lizardite spectrum. Though
497 contributing to the peak, this is unlikely to significantly alter the peak position.
498



499

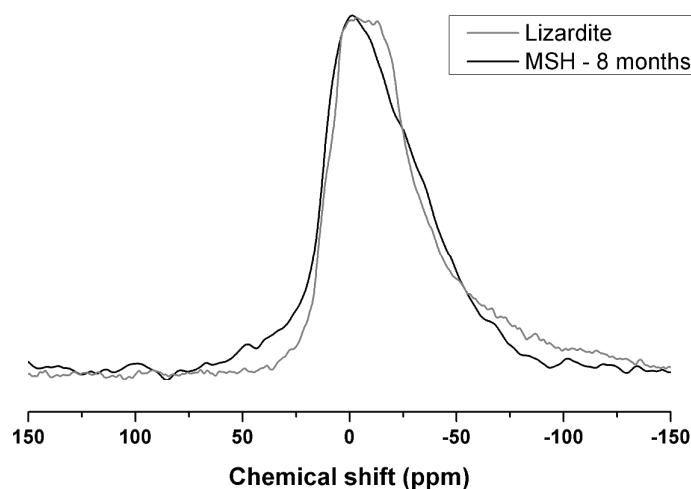
500 **Figure 12.** ^{25}Mg MAS NMR spectra of 1 and 8 month cured M-S-H with reference materials.

501 Note that the antigorite spin rate was increased from 10 to 14 kHz due to line broadening

502

from iron.

503



504

505 **Figure 13.** ^{25}Mg MAS NMR spectra of 8 month cured M-S-H, and comparison with lizardite

506

507 Studies of mineral formation in the M-S-H system have evolved significantly over time, as
508 thermodynamic and kinetic data are refined. Previous papers have included chrysotile as a
509 stable phase, or exclude lizardite from calculations, leading to predictions that either
510 antigorite or chrysotile are stable at low temperatures.⁴⁵ Recently, however, it has been
511 concluded that lizardite is the stable phase in the M-S-H system below ~ 300 °C, with
512 antigorite only stable at temperatures exceeding 250 °C.⁴⁶ Chrysotile is postulated to only
513 form from supersaturated solutions as a kinetic effect,⁴⁷ having no thermodynamically stable
514 range within the M-S-H field.⁴⁶ Given this assessment, it seems reasonable to conclude that
515 the serpentine-like feature in the M-S-H gel is likely to be structurally similar to the
516 thermodynamically most stable phase; this is lizardite, given the formation conditions.

517

518 This assignment fits well with the chemistry of the binders produced within the $\text{Mg}(\text{OH})_2$ -
519 SiO_2 - H_2O system studied; assuming complete reaction of $\text{Mg}(\text{OH})_2$ and SiO_2 in these
520 samples, the molar Mg/Si ratio of this binder should be ~ 0.95 . This ratio is between those of
521 talc (0.75) and lizardite (1.5), and thus suggests that the structural motifs of both mineral

522 types are likely to be present in the gel structure. It does, however, appear that ageing of the
523 gels produces a gel which is closer in structure to lizardite than talc, as evidenced by the
524 aforementioned NMR data.

525

526 Analysis of M-S-H gels at different Mg/Si ratios by Brew and Glasser^{14a} showed that
527 increasing the Mg/Si ratio of the M-S-H gel induced changes in the peak positions of the ²⁹Si
528 MAS NMR resonances towards less negative chemical shift values. In that study, aged M-S-
529 H gels formulated with Mg/Si ratios of 0.82 and 0.89 exhibited Q³ bands at chemical shifts of
530 -98.8 ppm and -97.7 ppm respectively, whereas M-S-H gels produced with an Mg/Si ratio of
531 0.94 showed a peak shifted to -94.6 ppm. The authors noted that their FTIR and ²⁹Si NMR
532 data more closely resembled chrysotile than talc. This suggests that there is a shift from the
533 formation of a poorly crystalline talc-like structure to a poorly crystalline serpentine-like
534 material when the Mg/Si ratio is increased. It is important to understand this structural shift as
535 a function of composition, as knowledge of the structure of the M-S-H can help to predict its
536 future behaviour, likely stability, and the quantity of Mg(OH)₂ which can be accommodated
537 into this system, and this is central to its use as a nuclear wasteform. The addition of
538 phosphate to enhance fluidity does not appear to significantly alter the final M-S-H structure,
539 although it retards the kinetics of conversion of amorphous silica to M-S-H in the first month
540 of curing.

541

542

543 **5. Conclusions**

544

545 Mg(OH)₂ has been successfully used to produce an M-S-H cement. The M-S-H produced was
546 similar to high-Mg gels described in other works, and largely consists of a poorly crystalline

547 serpentine-like assembly, which we have assigned as a lizardite-type structure. The addition
548 of $(\text{NaPO}_3)_6$ was effective in dispersing the $\text{Mg}(\text{OH})_2$ particles and adding fluidity to the
549 system. Higher doses of phosphate (2 wt.% or more) delay the formation of M-S-H, with 1
550 wt.% addition conferring the highest fluidity with minimal impact on M-S-H formation. The
551 developments presented in this work will enable M-S-H to be used as an encapsulant for both
552 low and high-water content sludges without the occurrence of bleed water, which would
553 otherwise need to be decanted and treated as a secondary waste stream if Portland cement-
554 based grouts were used to treat these sludges. The implementation of these cements for
555 Magnox sludge encapsulation is, however, likely to be hindered by slow strength
556 development in samples with a high water/binder ratio, despite providing an effective method
557 of converting this waste into a cementitious binder. Application of this cement would also be
558 highly dependent on the Mg/Si ratio in the resultant cementitious slurry. Retrieved sludges
559 can vary widely in their $\text{Mg}(\text{OH})_2$ contents. This study has highlighted the potential for
560 control of gel nanostructure depending on the Mg/Si ratio.

561

562

563 **6. Acknowledgements**

564

565 This study has been sponsored by the Engineering and Physical Sciences Research Council
566 through the University of Sheffield/ University of Manchester Doctoral Training Centre
567 ‘Nuclear FiRST’ and through a Nuclear Decommissioning Authority CASE award, under
568 supervision by the National Nuclear Laboratory. The donation of microsilica by ELKEM
569 Silicon Material (United Kingdom) is greatly appreciated. Solid-state NMR spectra were
570 obtained at the EPSRC UK National Solid-state NMR Service at Durham, and we are grateful
571 for the assistance of Dr David Apperley related to the experiments conducted at that facility.

572 The UK 850 MHz solid-state NMR Facility used in this research was funded by EPSRC and
573 BBSRC, as well as the University of Warwick including via part funding through
574 Birmingham Science City Advanced Materials Projects 1 and 2 supported by Advantage
575 West Midlands (AWM) and the European Regional Development Fund (ERDF). The input of
576 Dr Dinu Iuga in conducting experiments is also gratefully acknowledged

577

578

579 6. References

- 580 1. Nuclear Decommissioning Authority *Waste stream 2D95.1 Magnox fuel storage pond*
581 *sludge*; NDA: 2013.
- 582 2. Gregson, C. R.; Goddard, D. T.; Sarsfield, M. J.; Taylor, R. J., Combined electron
583 microscopy and vibrational spectroscopy study of corroded Magnox sludge from a legacy
584 spent nuclear fuel storage pond. *J. Nucl. Mater.* **2011**, *412* (1), 145-156.
- 585 3. Parry, S.; Livens, F.; O'Brien, L., Corroded Magnox sludge and plutonium waste
586 cementation. *Geochim. Cosmochim. Acta* **2007**, *71* (15, Supplement), A747-A815.
- 587 4. Nuclear Decommissioning Authority *Waste stream 2D16: Magnox fuel storage pond*
588 *sludge*; NDA 2007.
- 589 5. Atkins, M.; Glasser, F. P., Application of portland cement-based materials to
590 radioactive waste immobilization. *Waste Manag.* **1992**, *12* (2-3), 105-131.
- 591 6. Collier, N. C.; Milestone, N. B., The encapsulation of Mg(OH)₂ sludge in composite
592 cement. *Cem. Concr. Res.* **2010**, *40* (3), 452-459.
- 593 7. Hough, T.; Palethorpe, S., Development of a direct encapsulation technique for the
594 treatment of a mixed sludge / solid waste. In *WM'07 Conference*, Tucson, AZ, 2007.
- 595 8. Vandeperre, L. J.; Liska, M.; Al-Tabbaa, A., Microstructures of reactive magnesia
596 cement blends. *Cem. Concr. Compos.* **2008**, *30* (8), 706-714.
- 597 9. Gartner, E. M.; Macphee, D. E., A physico-chemical basis for novel cementitious
598 binders. *Cem. Concr. Res.* **2011**, *41* (7), 736-749.
- 599 10. Wilson, A. D.; Nicholson, J. W., *Acid-base cements - Their biomedical and industrial*
600 *applications*. Cambridge University Press: Cambridge, 1993.
- 601 11. Tooper, B.; Cartz, L., Structure and formation of magnesium oxychloride Sorel
602 cements. *Nature* **1966**, *211*, 64-66.

- 603 12. (a) Zhang, T.; Cheeseman, C. R.; Vandeperre, L. J., Development of low pH cement
604 systems forming magnesium silicate hydrate (M-S-H). *Cem. Concr. Res.* **2011**, *41* (4), 439-
605 442; (b) Szczerba, J.; Prorok, R.; Śnieżek, E.; Madej, D.; Maślona, K., Influence of time and
606 temperature on ageing and phases synthesis in the MgO–SiO₂–H₂O system. *Thermochim.*
607 *Acta* **2013**, *567*, 57-64; (c) Zhang, T.; Vandeperre, L. J.; Cheeseman, C., Bottom-up design of
608 a cement for nuclear waste encapsulation. In *Ceramic Materials for Energy Applications*,
609 John Wiley & Sons, Inc.: 2011; pp 41-49.
- 610 13. (a) Mitsuda, T., Paragenesis of 11 Å tobermorite and poorly crystalline hydrated
611 magnesium silicate. *Cem. Concr. Res.* **1973**, *3* (1), 71-80; (b) Mitsuda, T.; Taguchi, H.,
612 Formation of magnesium silicate hydrate and its crystallization to talc. *Cem. Concr. Res.*
613 **1977**, *7* (3), 223-230; (c) Takahashi, N.; Tanaka, M.; Satoh, T.; Endo, T., Study of synthetic
614 clay minerals. III. synthesis and characterization of two dimensional talc. *Bull. Chem. Soc.*
615 *Japan* **1994**, *67* (9), 2463-2467.
- 616 14. (a) Brew, D. R. M.; Glasser, F. P., Synthesis and characterisation of magnesium
617 silicate hydrate gels. *Cem. Concr. Res.* **2005**, *35* (1), 85-98; (b) Temujin, J.; Okada, K.;
618 MacKenzie, K. J. D., Formation of layered magnesium silicate during the aging of
619 magnesium hydroxide–silica mixtures. *J. Am. Ceram. Soc.* **1998**, *81* (3), 754-756.
- 620 15. (a) Wei, J.; Yu, Q.; Zhang, W.; Zhang, H., Reaction products of MgO and microsilica
621 cementitious materials at different temperatures. *J. Wuhan Univ. Technol. Mater. Sci. Ed.*
622 **2011**, *26* (4), 745-748; (b) Wei, J.; Chen, Y.; Li, Y., The reaction mechanism between MgO
623 and microsilica at room temperature. *J. Wuhan Univ. Technol. Mater. Sci. Ed.* **2006**, *21* (2),
624 88-91.
- 625 16. (a) Santhanam, M.; Cohen, M. D.; Olek, J., Mechanism of sulfate attack: A fresh
626 look: Part 1: Summary of experimental results. *Cem. Concr. Res.* **2002**, *32* (6), 915-921; (b)
627 Bonen, D.; Cohen, M. D., Magnesium sulfate attack on portland cement paste — II.
628 Chemical and mineralogical analyses. *Cem. Concr. Res.* **1992**, *22* (4), 707-718.
- 629 17. Brew, D. R. M.; Glasser, F. P., The magnesia-silica gel phase in slag cements: alkali
630 (K, Cs) sorption potential of synthetic gels. *Cem. Concr. Res.* **2005**, *35* (1), 77-83.
- 631 18. Corkhill, C. L.; Cassingham, N. J.; Heath, P. G.; Hyatt, N. C., Dissolution of UK
632 high-level waste glass under simulated hyperalkaline conditions of a colocated geological
633 disposal facility. *Int. J. Appl. Glass Sci.* **2013**, *4* (4), 341-356.
- 634 19. García Calvo, J. L.; Hidalgo, A.; Alonso, C.; Fernández Luco, L., Development of
635 low-pH cementitious materials for HLRW repositories: Resistance against ground waters
636 aggression. *Cem. Concr. Res.* **2010**, *40* (8), 1290-1297.
- 637 20. (a) Young, A. J.; Warwick, P.; Milodowski, A. E.; Read, D., Behaviour of
638 radionuclides in the presence of superplasticiser. *Adv. Cem. Res.* **2013**, *25* (1), 32-43; (b)
639 Clacher, A. P.; Cowper, M.M., *Effect of ADVA cast 551 on the solubility of plutonium(IV)*
640 *and uranium(VI)*; Serco Report SERCO/TAS/003145/001 to NDA RWMD, Harwall, UK
641 2011.
- 642 21. (a) Otrój, S.; Bahrevar, M. A.; Mostarzadeh, F.; Nilforoshan, M. R., The effect of
643 deflocculants on the self-flow characteristics of ultra low-cement castables in Al₂O₃–SiC–C
644 system. *Ceram. Int.* **2005**, *31* (5), 647-653; (b) Andreola, F.; Castellini, E.; Lusvardi, G.;

- 645 Menabue, L.; Romagnoli, M., Release of ions from kaolinite dispersed in deflocculant
646 solutions. *Appl. Clay Sci.* **2007**, *36* (4), 271-278.
- 647 22. Kantro, D. L., Influence of water-reducing admixtures on properties of cement paste -
648 a miniature slump test. *Cem., Concr. Aggr.* **1980**, *2* (2), 95-102.
- 649 23. Rasband, W. S. *ImageJ*, 1.48; U. S. National Institutes of Health: Bethesda,
650 Maryland, 2014.
- 651 24. Ojovan, M. I.; Lee, W. E., *An introduction to nuclear waste immobilisation*. Elsevier:
652 Oxford, 2005.
- 653 25. NDA, *WPS/700: 500 litre drum waste package specifications: explanatory material*
654 *and design guidelines*; Nuclear Decommissioning Authority, UK, 2008.
- 655 26. Liao, J.; Senna, M., Thermal behavior of mechanically amorphized talc. *Thermochim.*
656 *Acta* **1992**, *197* (2), 295-306.
- 657 27. Suquet, H., Effects of dry grinding and leaching on the crystal structure of chrysotile.
658 *Clays Clay Miner.* **1989**, *37* (5), 439-445.
- 659 28. MacKenzie, K. J. D.; Meinhold, R. H., The thermal reactions of talc studied by ²⁹Si
660 and ²⁵Mg MAS NMR. *Thermochim. Acta* **1994**, *244*, 195-203.
- 661 29. (a) Aglietti, E. F., The effect of dry grinding on the structure of talc. *Appl. Clay Sci.*
662 **1994**, *9* (2), 139-147; (b) Drief, A.; Nieto, F., The effect of dry grinding on antigorite from
663 Mulhacen, Spain. *Clays Clay Miner.* **1999**, *47* (4), 417-424.
- 664 30. Smykatz-Kloss, W., *Differential thermal analysis. Application and results in*
665 *mineralogy*. Springer-Verlag: Berlin, 1974.
- 666 31. Sharp, J. H.; Wilburn, F. W.; McIntosh, R. M., The effect of procedural variables on
667 TG, DTG and DTA curves of magnesite and dolomite. *J. Thermal Anal.* **1991**, *37* (9), 2021-
668 2029.
- 669 32. Viti, C., Serpentine minerals discrimination by thermal analysis. *Am. Miner.* **2010**, *95*
670 (4), 631-638.
- 671 33. (a) Lippincott, E. R.; Valkenburg, A. V.; Weir, C. E.; Bunting, E. N., Infrared studies
672 on polymorphs of silicon dioxide and germanium dioxide. *J. Res. Natl. Bureau Standards*
673 **1958**, *61* (1), 61-70; (b) Ocaña, M.; Fornés, V.; Serna, C. J., The variability of the infrared
674 powder spectrum of amorphous SiO₂. *J. Non-Cryst. Solids* **1989**, *107* (2-3), 187-192.
- 675 34. (a) Ryskin, Y. I., The vibrations of protons in minerals: hydroxyl, water and
676 ammonium. In *The Infrared Spectra of Minerals*, Farmer, V. C., Ed. Mineralogical Society:
677 London, 1974; pp 137-182; (b) Chukanov, N., *Infrared spectra of mineral species*. Springer
678 Netherlands: 2014; p 21-1701.
- 679 35. Farmer, V. C., The layer silicates. In *The infrared spectra of minerals*, Farmer, V. C.,
680 Ed. Mineralogical Society: London, 1974; pp 331-364.

- 681 36. Russell, J. D.; Farmer, V. C.; Velde, B., Replacement of OH by OD in layer silicates,
682 and identification of the vibrations of these groups in infra-red spectra. *Miner. Mag.* **1970**, *37*
683 (292), 869-879.
- 684 37. d'Espinose de la Caillerie, J.-B.; Kermarec, M.; Clause, O., ^{29}Si NMR observation of
685 an amorphous magnesium silicate formed during impregnation of silica with Mg(II) in
686 aqueous solution. *J. Phys. Chem.* **1995**, *99* (47), 17273-17281.
- 687 38. MacKenzie, K. J. D.; Meinhold, R. H., Thermal reactions of chrysotile revisited: A
688 ^{29}Si and ^{25}Mg MAS NMR study. *Am. Miner.* **1994**, *79*, 43-50.
- 689 39. (a) Kosuge, K.; Shimada, K.; Tsunashima, A., Micropore formation by acid treatment
690 of antigorite. *Chem. Mater.* **1995**, *7* (12), 2241-2246; (b) Nakata, S.; Asaoka, S.; Kondoh, T.;
691 Takahashi, H., Characterization of natural zeolites and clay minerals by high-resolution solid-
692 state NMR. *Nendo Kagaku* **1986**, *26*, 197-208.
- 693 40. Hilbig, H.; Köhler, F. H.; Schiebl, P., Quantitative ^{29}Si MAS NMR spectroscopy of
694 cement and silica fume containing paramagnetic impurities. *Cem. Concr. Res.* **2006**, *36* (2),
695 326-329.
- 696 41. (a) Mellini, M., The crystal structure of lizardite 1T: hydrogen bonds and polytypism.
697 *Am. Miner.* **1982**, *67*, 587-598; (b) Trittschack, R.; Grobety, B., Dehydroxylation kinetics of
698 lizardite. *Eur. J. Miner.* **2012**, *24* (1), 47-57; (c) Caruso, L. J.; Chernosky, J. V., The stability
699 of lizardite. *Can. Miner.* **1979**, *17* (4), 757-769.
- 700 42. Pallister, P. J.; Moudrakovski, I. L.; Ripmeester, J. A., Mg-25 ultra-high field solid
701 state NMR spectroscopy and first principles calculations of magnesium compounds. *Phys.*
702 *Chem. Chem. Phys.* **2009**, *11* (48), 11487-11500.
- 703 43. (a) Cahill, L. S.; Hanna, J. V.; Wong, A.; Freitas, J. C. C.; Yates, J. R.; Harris, R. K.;
704 Smith, M. E., Natural abundance ^{25}Mg solid-state NMR of Mg oxyanion systems: A
705 combined experimental and computational study. *Chem. Eur. J.* **2009**, *15* (38), 9785-9798;
706 (b) Ashbrook, S. E.; Sneddon, S., New methods and applications in solid-state nmr
707 spectroscopy of quadrupolar nuclei. *J. Am. Chem. Soc.* **2014**, *136* (44), 15440-15456; (c)
708 Laurencin, D.; Gervais, C.; Stork, H.; Krämer, S.; Massiot, D.; Fayon, F., ^{25}Mg solid-state
709 NMR of magnesium phosphates: high magnetic field experiments and density functional
710 theory calculations. *J. Phys. Chem. C* **2012**, *116* (37), 19984-19995; (d) Freitas, J. C. C.;
711 Smith, M. E., Recent advances in solid-state ^{25}Mg NMR spectroscopy. In: *Annual Reports on*
712 *NMR Spectroscopy*, Graham, A. W., Ed. Academic Press: 2012; Vol. 75, pp. 25-114.
- 713 44. Slichter, C. P., *Principles of magnetic resonance*. 3rd ed.; Springer-Verlag: Berlin,
714 1996.
- 715 45. (a) O'Hanley, D. S.; Wicks, F. J., Conditions of formation of lizardite, chrysotile and
716 antigorite, Cassiar, British Columbia. *Can. Miner.* **1995**, *33*, 753-773; (b) Day, H. W.;
717 Chernosky, J. V.; Kumin, H. J., Equilibria in the system MgO-SiO₂-H₂O: a thermodynamic
718 analysis. *Am. Miner.* **1985**, *70*, 237-248.
- 719 46. Evans, B. W., The serpentinite multisystem revisited: chrysotile is metastable. *Int.*
720 *Geol. Rev.* **2004**, *46*, 479-506.

721 47. (a) Peters, E. K., D-¹⁸O enriched waters of the Coast Range Mountains, northern
722 California: Connate and ore-forming fluids. *Geochim. Cosmochim. Acta* **1993**, *57*, 1093-
723 1104; (b) Nesbitt, H. W.; Bricker, O. P., Low temperature alteration process affecting
724 ultramafic bodies. *Geochim. Cosmochim. Acta* **1978**, *42*, 403-409.

725

726